Basal Plane Activation in Monolayer $MoTe_2$ for Hydrogen Evolution Reaction via Phase Boundaries

Yiqing Chen, Pengfei Ou, Xiaohan Bie, Jun Song*

Department of Mining and Materials Engineering, McGill University, Montreal H3A 0C5, Canada

ABSTRACT

Two-dimensional transition metal dichalcogenides (2D TMDCs) have attracted tremendous interest as one prominent material group promising inexpensive electrocatalysts for hydrogen evolution reaction (HER). In the present study, using monolayer $MoTe_2$ as a representative, we demonstrated that phase boundaries can provide a viable pathway to activate the basal plane of 2D TMDCs for enhanced HER performance. Comprehensive first-principles calculations have been performed to examine the energetics and structural stabilities of possible 2H/1T' phase boundary configurations. Three categories of sites, Te, Mo and hollow sites, have been identified in energetically stable phase boundaries, as potential catalytic centers for HER, all indicating enhanced HER activity than the pristine basal lattice. In particular, the hollow sites, a new group of sites induced by phase boundaries, show great promise by exhibiting a Gibbs free energy (ΔG_H) near the thermoneutral value for hydrogen adsorption, comparable to that of Pt. The mechanisms underlying hydrogen adsorption at phase boundaries were then revealed, shown to be attributed to the unique local hydrogen adsorption geometries and electronic structures at phase boundaries. Our study clarifies the important mechanistic aspects underlying hydrogen activation at phase boundaries, providing valuable theoretical insights towards designing new class of high-performance HER electrocatalysts based on 2D TMDCs.

INTRODUCTION

Electrochemical water splitting is of particular importance to the production of hydrogen, crucial for the global goal towards clean energy economy and sustainability [1]. One core challenge

in research efforts on water splitting is to identify efficient catalysts to facilitate evolution of H_2, i.e. hydrogen-evolution reaction (HER). Currently, platinum (Pt) and Pt-based materials are regarded as the *de facto* standard catalysts for HER, but suffer high cost and material scarcity, which hinder their large-scale utilization [2-3]. Therefore, there have been great efforts for alternative, non-Pt catalysts with low cost and high performance [4]. Among various potential non-Pt catalyst candidates, monolayer transition-metal dichalcogenides (TMDCs) are found to be effective towards HER [5-8]. For instance, theoretical and experimental studies have suggested that monolayer MoS_2 can catalyze HER at a moderate overpotential of 0.1-0.2 V with Gibbs free energy of adsorption close to zero (<0.1 eV) at its edge sites [9].

However, for monolayer TMDCs, the active sites for HER are limited to the edge sites while the basal plane is inert, rendering large surface area catalytically useless [10-11]. Such limitation has motivated a great quest aiming to activate the basal plane of TMDCs. One popular method resulted from the quest is the introduction of (point) defects in TMDCs, which has been shown to lead to significant enhancement in HER activity [10, 12-14]. Yet, with the introduction of defects come the abundant dangling bonds at defect sites, which may poison the HER reaction and cause structural instabilities [15]. A few other studies have suggested the approach of transforming TMDCs from the semiconducting 2H phase to metallic 1T(or 1T') phase. This 2H→1T(1T') phase transformation is shown to provide numerous active sites in the basal plane and at the same time improves the electrical conductivity of TMDCs [16-18]. However, the 1T(1T') phase of most TMDCs is metastable and can easily revert back to the 2H phase [19]. More recently, Zhu et al. demonstrated from their experimental study that the basal plane of monolayer MoS_2 can be activated by introducing phase boundaries [15]. This facile route can provide a high density of active sites while retaining the structural stability by 2H-1T phase integration [20]. It hints promising new avenues towards basal plane activation of TMDCs without deteriorating the structural stability.

Meanwhile it is worth noting that, for group-VI TMDCs, 1T' phase is energetically more favourable than 1T phase. Therefore it is reasonable to expect that, compared to 2H/1T phase boundaries, 2H/1T' phase boundaries would be thermodynamically more preferable, and be more are more likely to meets the requirement for structural stability and large-scale synthesis. Among the big family of monolayer TMDCs, $MoTe_2$ is an appealing candidate for achieving 2H/1T' phase boundaries [21-23] because of small energy difference between the 2H and 1T' phases [22]. Therefore

thermodynamically it is expected that the phase boundaries in $MoTe_2$ are relatively easy to form, and indeed they have already been successfully synthesized by chemical vapor deposition (CVD) [24] and heteroepitaxy [21]. Previous studies have also shown that $MoTe_2$ phase boundaries exhibit excellent electrical properties [24-26], an important factor that influences the overall catalytic activity towards HER [27]. The high conductivity of $MoTe_2$ and neglectable contact resistance at the boundaries contribute to a fast electron transfer speed [27-29] and holds promise for the engineering of high-performance electrocatalysts in the future.

However, in contrast to the numerous studies on isolated defects and edges in TMDCs with respect to HER, research work on phase boundaries has been rather scarce, except for some recent studies examining specific phase boundaries in MoS_2 to show the existence of active sites on S atoms for hydrogen adsorption to potentially enhance HER activity [15, 30]. Consequently, knowledge regarding HER at phase boundaries in TMDCs remains largely absent, necessitating dedicated studies. Aiming at such need, here in this paper, we perform systematic density functional theory (DFT) calculations to investigate HER activities at phase boundaries in $MoTe_2$ as a representative TMDC system. Possible 2H/1T' phase boundaries are constructed to examine their structural stabilities. Various candidate adsorption sites, namely Te, Mo and hollow sites, are explored on the stable configurations. Our calculations show that all adsorption sites at $MoTe_2$ phase boundaries are activated, with the hollow sites as the most active sites for HER and exhibiting outstanding HER activity comparable to that of Pt. Besides, we propose mechanisms to understand such activation at the phase boundaries. Hydrogen adsorptions at the Te sites are interpreted and predicted by Fermi-abundance (D_F) model while the adsorption at Mo and hollow sites are qualitatively understood by analyzing the local charge distribution and density of states. The HER activity at the phase boundary was shown to be strongly dependent on the local hydrogen adsorption geometry and electronic structures.

METHOD AND MODEL

Monolayer $MoTe_2$ has three polymorphs, semiconducting 2H phase, and metallic 1T and 1T' phases. Figs. 1(a) and 1(b) show the trigonal prismatic 2H phase consisting of 1×1 unit cells, and the distorted octahedral 1T' phase with zigzag chains consisting of 2×1 supercells. It is worth to

note that the 1T phase of $MoTe_2$ is metastable and would readily transform into the 1T' phase, and therefore is not discussed in our study. On base of 2H and the 1T' phases, a series of 2H/1T' phase boundaries are constructed (details see Supporting Information S2). In describing the phase boundaries, the name convention used in the study of Zhao et al. [31] is used but modified accordingly to fit our 2H/1T' case. A phase boundary is thus named using the form of $D_M(-A-B)|S$, where D represents the direction of a $MoTe_2$ phase boundary, being zigzag (ZZ) or armchair (AC), with its subscript M denoting the type of the atoms (Te or Mo) shared by two phases at the boundary, and S indicates whether the phase boundary is rich in Te ($S = +$) or deficient in Te ($S = -$). A and B represent the types of edge configurations for 2H and 1T' nanoribbons respectively at the phase boundary. There are four edge configurations, i.e., α, β, C and T for a phase boundary along the ZZ direction (See Fig. 1(a)-(b)). On the other hand, since all phase boundaries along the AC direction have the same edge configurations, the form thus simplifies to become $AC_M|S$ only.

Fig. 1(c) shows configurations of those stable phase boundary structures after geometry relaxation. Fig. 1(d) further illustrates a couple of sample relaxed structures of ZZ and AC phase boundaries in both top and side views. It is worth noting that for ZZ phase boundaries, the D_{3h} symmetry of 2H MoS_2 inevitably leads to different edge structures at both ends of a 2H MoS_2 nanosheet. Thus, periodicity along the ZZ direction would mandate two different phase boundaries (details see Supporting Information), which however would make accurate evaluation of the phase boundary formation energy difficult. To address such challenge, for ZZ phase boundaries, we construct a nanoribbon-like structure instead of a fully periodic sheet, as suggested in the study of Zhou et al. [32], containing one phase boundary in the middle while one 2H edge and one 1T' edge at each end. The dimension of the vacuum space along the non-periodic direction is set to be larger than 20Å to ensure no image interaction. Meanwhile benchmark calculations have been performed to ensure that the separation between the nanoribbon edges is sufficiently large to avoid any artificial effect arising from edge-edge or edge-boundary interactions (details see Supporting Information). On the other hand, for AC phase boundaries, periodicity along the AC direction can be satisfied, and thus a periodic sheet rather than nanoribbon is adopted as the model structure.

All DFT calculations were performed employing the VIENNA ab initio simulation package (VASP) [33-34] using the projector-augmented wave method [35]. The exchange-correlation functional was described by generalized gradient approximation (GGA) parametrized by Perdew, Burke, and

Ernzerhof [36-37]. A kinetic cutoff energy of 550 eV was set for the plane-wave basis functions. All structures were relaxed until the atomic forces are less than 0.01 eV/Å and total energies were converged to 10^{-5} eV. Given that hydrogen adsorption and HER characteristics would be affected by hydrogen coverage, we considered different hydrogen coverages, ranging from 25% to 100%. Nonetheless, for simplicity and clarity of presentation, below the results presented mostly correspond to a hydrogen coverage of 50%. Additionally, in the calculations of hydrogen adsorption, the effect of van der Waals (vdW) interactions was included using DFT-D3 method [38-39].

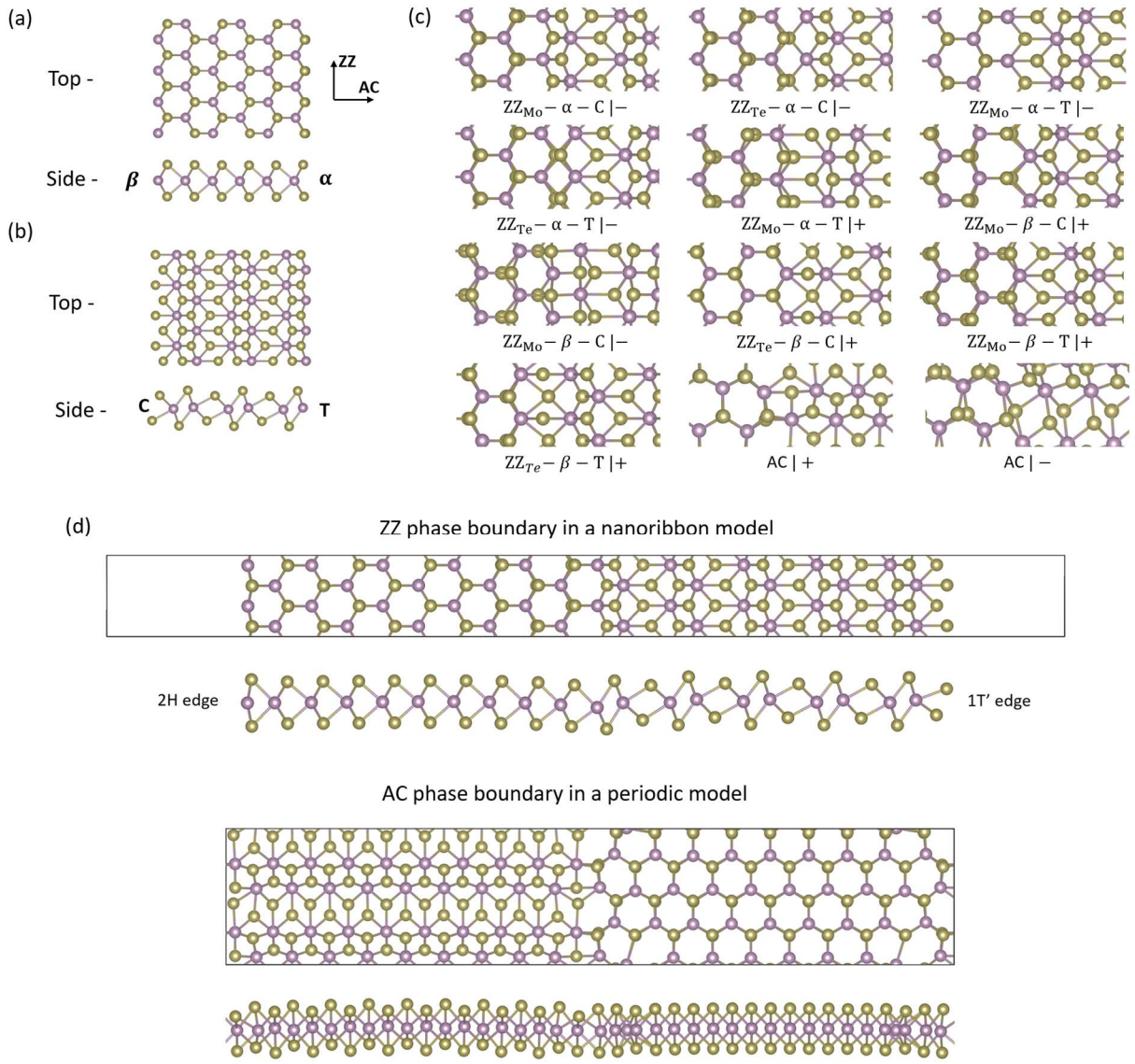

Fig. 1 The top and side views of pristine (a) 2H and (b) 1T' $MoTe_2$, where Mo atoms are shown in purple and Te atoms are shown in brown, with the black arrows indicating the AC and ZZ directions of $MoTe_2$ lattice. Two types of 2H edges (i.e., α and β) and 1T' edges ((i.e., C and T) are indicated on the side views. (c) The relaxed configurations of the twelve 2H/1T' phase boundaries examined, named following the convention suggested by Zhao et al. [31]. (d) The top and side views of a representative ZZ phase boundary, $ZZ_{Mo}-\alpha-C|-$ embedded in a nanoribbon model with 2H and 1T' edges at each side, and an AC phase boundary $AC|+$ embedded in a periodic sheet model.

RESULTS AND DISCUSSION

Formation energies of $MoTe_2$ phase boundaries. Before evaluating hydrogen adsorption and HER at $MoTe_2$ phase boundaries, we first investigate the formation energies of phase boundaries. For a ZZ phase boundary, its formation energy E_f can be determined from the total energy of the structure E_T as the following [23]:

$$E_T = N_{Mo}\mu_{Mo} + N_{Te}\mu_{Te} + L(\sigma_H + \sigma_{T'} + E_f) \quad (1)$$

where N_{Mo} and N_{Te} are the numbers of Mo and Te atoms in the phase boundary respectively, L is the phase boundary length, σ_H and $\sigma_{T'}$ are the formation energies of 2H and 1T' edges per unit length, which can be obtained from separate calculations (details see Supporting Information), and μ_{Mo} and μ_{Te} are the chemical potentials of Mo and Te respectively. To maintain thermodynamic equilibrium, the allowable range of μ_{Te} and μ_{Mo} are constraint by the following condition:

$$\mu_{MoTe2} = \mu_{Mo} + 2\mu_{Te} \quad (2)$$

where μ_{MoTe2} represents the average weighted chemical potential of 2H and 1T' phases. μ_{Te} varies depending on the chemical environment, assuming higher and lower values under Te-rich and Mo-rich conditions, respectively. The upper and lower limits of μ_{Te} can be regarded as being defined by the chemical potentials of alpha Te and body-centered cubic Mo respectively, thus ranging from -3.54 eV to -3.14 eV. The details of formation energy calculation can be found in Supporting Information.

For AC phase boundaries, periodic structures are constructed (cf. Fig. 1d), and the total energy of the structure can be written as:

$$E_T = N_{Mo}\mu_{Mo} + N_{Te}\mu_{Te} + 2E_f L \quad (3)$$

From Eqs. (1) and (3), the formation energy E_f can then be determined. The E_f values of various phase boundaries as functions of μ_{Te} are shown in Fig. 2. The lowest energy phase boundary is found to be $ZZ_{Mo} - \alpha - C|-$ boundary under Mo-rich conditions ($-3.54\ eV < \mu_{Te} < -3.27\ eV$), while it becomes the $ZZ_{Mo} - \beta - T|+$ boundary when the environment becomes Te-rich ($-3.27\ eV \leq \mu_{Te} < -3.14\ eV$). These results are in agreement with the recent studies on ZZ phase boundaries of $MoTe_2$ [23]. Further analyses reveal that the formation energy of a phase boundary is strongly correlated with the local bond distortion. For instance, $ZZ_{Te} - \beta - C|+$

boundary, the one with the highest formation energy, exhibits the most significant Mo-Te bond elongation/shrinkage at the boundary (see Fig. S3 in Supporting Information). This large bond length variation induces significant mechanical stress/strain, leading to increase in the formation energy. In comparison, the bond distortion in low formation energy boundaries, e.g., $ZZ_{Mo} - \beta - C| -$ boundary, is much moderate (see Fig. S3). It is also worthy to note from Fig. 2 that phase boundaries rich in Te ($S = +$) and deficient in Te ($S = -$) show opposite dependence on μ_{Te}, i.e., E_f respectively increasing and decreasing monotonically as μ_{Te} increases. Such opposite dependence is directly related to the sign of N_{Te} value, which is positive and negative for phase boundaries rich in Te ($S = +$) and deficient in Te ($S = -$) respectively.

With lower formation energy indicative of better stability and easier formation, consequently below we only consider the two low-energy boundaries, i.e., $ZZ_{Mo} - \alpha - C| -$ and $ZZ_{Mo} - \beta - T| +$ for our investigation on HER activities.

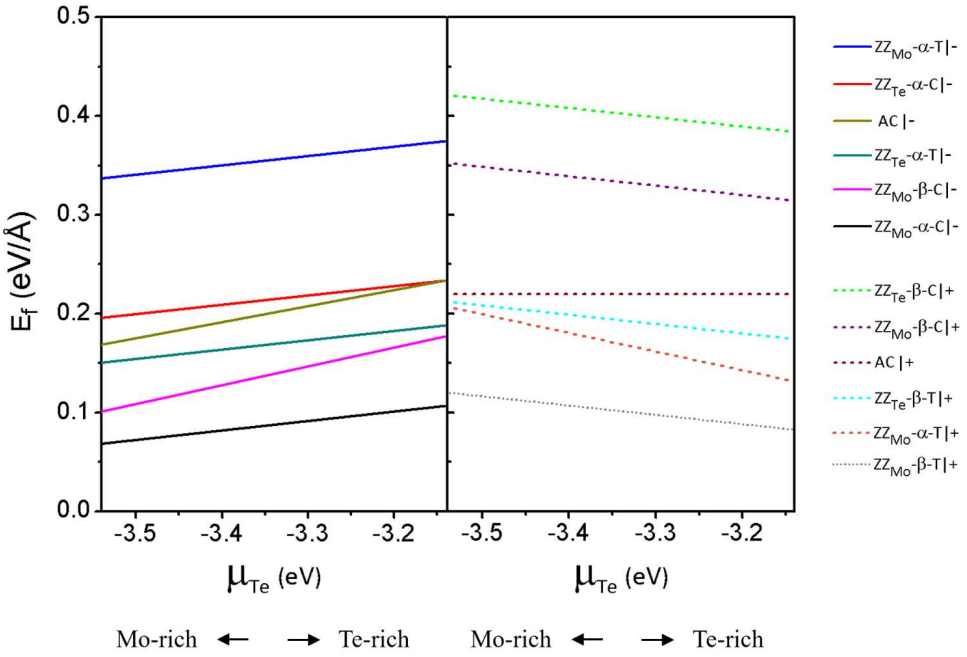

Fig. 2 Formation energies of the phase boundaries as functions of the chemical potential of Te, μ_{Te}.

Hydrogen adsorption at $MoTe_2$ phase boundaries. To investigate HER at the two phase boundaries of $ZZ_{Mo} - \alpha - C| -$ and $ZZ_{Mo} - \beta - T| +$, we first identify the possible hydrogen adsorption sites at the boundary. Those sites are illustrated in Fig. 3(a) and (c). As seen

from the figure, we note that at the vicinity of the phase boundary hydrogen may adsorb at the hollow site, or immediately above Mo or Te atoms. For simplicity in describing those adsorption sites, below we refer to the hollow site as HL, while the sites immediately above Mo or Te atoms as X_n where X = Mo or Te and n is an integer indicating the n^{th} site associated with X atom. In comparison to those sites at phase boundaries, their corresponding counterparts in pristine 2H and 1T' lattices of $MoTe_2$ are also identified (illustrated in Figure S4, see Supporting Information) and examined as the respective reference sites.

One of the first steps of HER is hydrogen adsorption at the electrode surface. Generally, to achieve good catalytic performance, the binding between hydrogen and the electrode surface should be neither too strong nor too weak. In accordance, it is desirable for hydrogen adsorption have a Gibbs free energy ΔG_H close to the thermoneutral value near zero. The Gibbs free energy ΔG_H can be calculated as follows [40]:

$$\Delta G_H = \Delta E_H + \Delta E_{ZPE} - T\Delta S_H \tag{4}$$

where ΔE_H is the adsorption energy of the n^{th} H atom and is defined as:

$$\Delta E_H = E_{MoTe_2+nH} - E_{MoTe_2+(n-1)H} - \frac{1}{2}E_{H_2} \tag{5}$$

where E_{MoTe_2+nH} is the total energy of $MoTe_2$ phase boundary with adsorbed hydrogen atoms, $E_{MoTe_2+(n-1)H}$ is the total energy of $MoTe_2$ phase boundary without adding a hydrogen atom, and E_{H_2} is the energy of a gas phase hydrogen molecule. ΔE_{ZPE} is the difference in zero-point energy of hydrogen in the adsorbed state and the gas phase. Our benchmark calculations have confirmed that vibrational frequencies do not differ notably for different hydrogen coverages and structures, and that there is little variation in ΔE_{ZPE}. Consequently ΔE_{ZPE} is simply taken to be a constant value (i.e., 0.02 eV). ΔS_H is the entropy term approximated as half of entropy of the gas phase H_2 as $\Delta S_H \approx \frac{1}{2}S_{H_2}$ [41]. T is the temperature, taken to be the room temperature ($T = 298\,K$) in our study. Under ambient conditions, the term $T\Delta S_H$ approximately assumes a value of 0.2 eV and thus Eq. (4) becomes:

$$\Delta G_H = \Delta E_H + 0.22 \text{ eV} \tag{6}$$

The Gibbs free energies of hydrogen adsorption at various sites in the boundary regions of $ZZ_{Mo} - \alpha - C| -$ and $ZZ_{Mo} - \beta - T| +$ respectively were examined. These values are presented in Fig. 3(b) and (d), in comparison with corresponding energies at the respective counterpart sites on pristine 2H or 1T' $MoTe_2$. As mentioned earlier in Section 2, the results correspond to a hydrogen coverage of 50%. It should be noted that Mo atoms connecting the 2H and 1T' phases of $MoTe_2$ at the boundary have two corresponding sites from pristine 2H and 1T' $MoTe_2$ respectively, in which case only the site of lower ΔG_H is considered for comparison. It is apparent from Fig. 3 that phase boundaries render ΔG_H lower and closer to zero compared to pristine 2H or 1T' $MoTe_2$, indicative of improved HER activity at the phase boundary. Moreover, examining the difference in adsorption energy (between a site at the phase boundary and its reference site in the pristine 2H or 1T' lattice), we note that the difference is more significant for sites on the 2H phase side. One salient observation from Fig. 3 is that hollow sites at phase boundaries exhibit near-zero ΔG_H values, in sharp contrast to their counterparts in the pristine $MoTe_2$. In particular, ΔG_H of the hollow site in $ZZ_{Mo} - \alpha - C| -$ shows a negative value close to zero ($\Delta G_H = -0.10\ eV$), exhibiting strong adsorption of hydrogen, which is comparable to that of Pt ($\Delta G_H = -0.09\ eV$) [12]. These results suggest that hollow sites at phase boundaries may promise drastic boost to the HER activity.

To further evaluate the implication of the phase boundary to HER performance, a volcano curve is plotted as shown in Fig. 3(e). In the plot, the theoretical exchange current density i_0 is calculated based on the Gibbs free energy ΔG_H. Adsorption sites with a negative ΔG_H are located around the left leg of the volcano, and the i_0 at pH 0 can be calculated by the following expression:

$$i_0 = -ek_0 \frac{1}{1 + exp(-\Delta G_H / k_B T)} \tag{7}$$

where k_0 is the rate constant with a value of 200 $s^{-1} site^{-1}$ fitted to give a reasonable overall magnitude of the rate, and k_B is the Boltzmann constant. For the other case where adsorption sites are located around the right leg of the volcano (ΔG_H is positive), the i_0 is given by:

$$i_0 = -ek_0 \frac{1}{1 + exp(-\Delta G_H / k_B T)} exp(-\Delta G_H / k_B T) \tag{8}$$

Adsorption sites with ΔG_H close to zero are located at the peak of the volcano curve, indicating the highest exchange current density and the optimal HER performance. We find that two hollow sites are located very close to the peak of the volcano curve with a very high exchange current density, suggesting them as the potential sites to offer best performance at the boundaries. Meanwhile, the influence of hydrogen coverage on ΔG_H is illustrated in Fig. 3(f). As seen in the figure, with the sites HL1, Mo2 and Te1 as representatives, we see that ΔG_H as a function of hydrogen coverage, exhibits a similar trend for different adsorption sites with the hollow sites always remaining to be the ones with the smallest $|\Delta G_H|$ values. As the hydrogen coverage increases, ΔG_H first increases till a coverage ~70%, followed by a slight decrease with further increase in the coverage. In particular, for the HL1 site shown in Fig. 3(f), one can see that the free energy close to zero occurs around 50%-60% hydrogen coverage, indicative of an optimal coverage for HER. Increasing hydrogen coverage beyond this range would increase ΔG_H (>0) for all sites, thus expected to lower the HER activity. On the other hand, decreasing hydrogen coverage below this range, though negatively impacting the hollow sites, renders the ΔG_H values of other sites closer to zero. Therefore, Fig. 3(f) also suggests more effective HER performance with hydrogen adsorption below 60% coverage.

Overall, our calculations above confirmed that phase boundaries in $MoTe_2$ can provide active sites with significantly better hydrogen adsorption characteristics, thus potentially contributing to boosting the overall HER performance of $MoTe_2$.

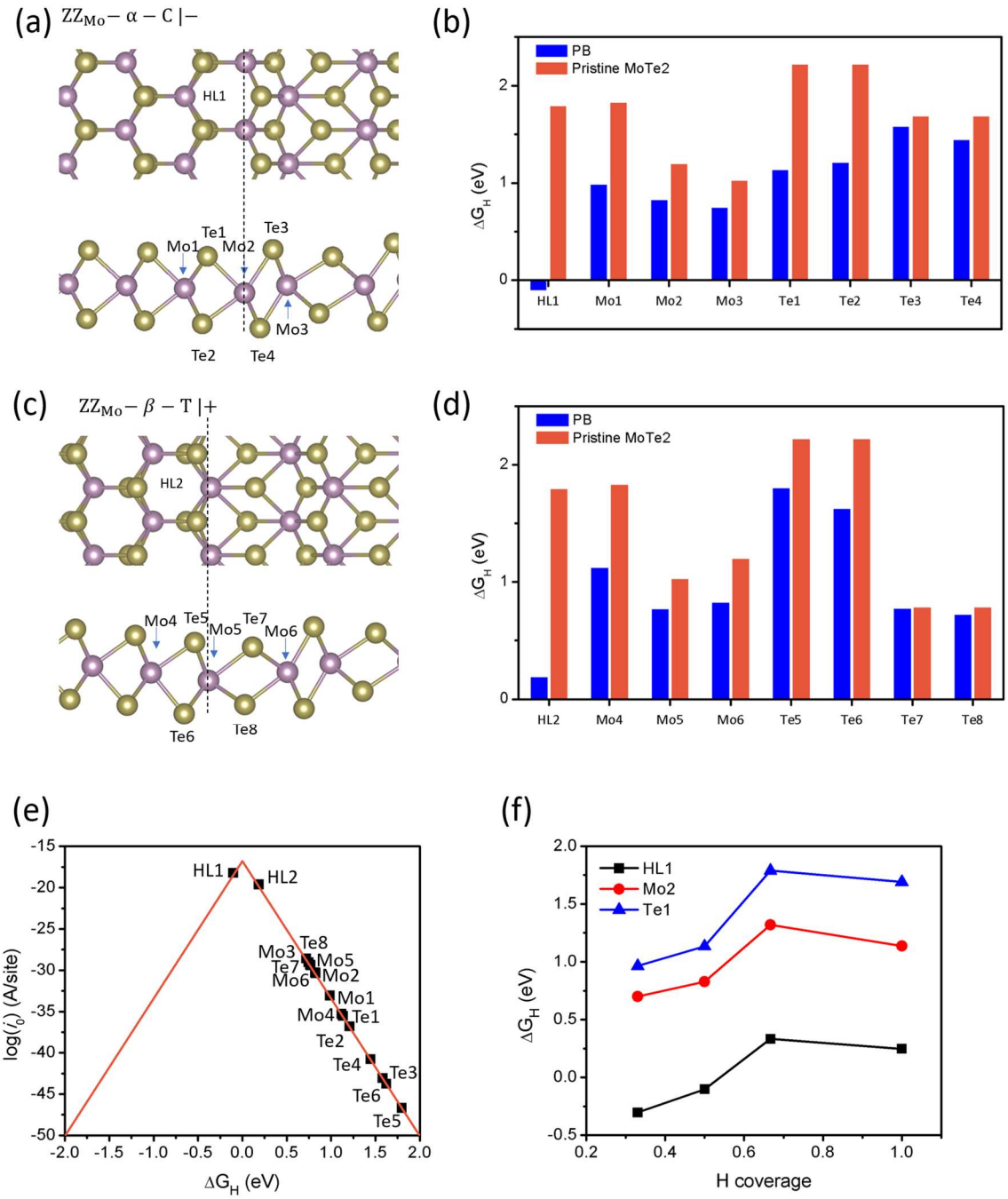

Fig 3. (a), (c) Adsorption sites of $ZZ_{Mo} - \alpha - C| -$ and $ZZ_{Mo} - \beta - T| +$ phase boundaries respectively. Adsorption sites are labeled by as Hollow (HL), Mo, and Te categories, respectively. (b), (d) ΔG_H values of $ZZ_{Mo} - \alpha - C| -$ and $ZZ_{Mo} - \beta - T| +$ phase boundaries, compared with the respective adsorption energies on pristine $MoTe_2$ at the representative hydrogen coverage of 50%. (e) Volcano plot between the

theoretical exchange current density i_0 and Gibbs free energy ΔG_H. (f) ΔG_H as a function of hydrogen coverage for three sites, HL1, Mo2 and Te1.

Relation of hydrogen adsorption to electronic properties. The key characteristics of a catalyst are fundamentally prescribed by their electronic structures. In this regard, we have performed comprehensive analysis of the electronic structures of those phase boundaries containing $MoTe_2$ systems to further understand the interaction between hydrogen and the various adsorption sites at the phase boundary. Generally, not every electronic state in the band contributes equally to the bonding between hydrogen and adsorption site. Huang et al. revealed that the closer an electronic state is to the Fermi level (E_F), the greater its contribution to the bonding [42]. Examining the density of states (DOS), we analyzed the states associated with different adsorption sites, with reference to the Fermi level. Some sample analysis is shown in Fig. 4(a), where the two Te adsorption sites, Te1 and Te5 (cf. Fig. 3), are compared (DOS of other Te sites are also examined, see Fig. S6 in Supporting Information). As noted from the figure, the Te1 site has more occupied states near the E_F compared to Te5, thus expected to have stronger hydrogen adsorption. This prediction based on the electronic analysis agrees well with the ΔG_H results, i.e., $\Delta G_{H-Te1} = 1.13$ eV < $\Delta G_{H-Te5} = 1.80$ eV (cf. Fig. 3 above).

To further quantitatively understand the relation between ΔG_H and the electronic structure, we note that, according to the Fermi-abundance (D_F) model [13, 42-43], the band structures of adsorption sites can be described by the following descriptor:

$$D_F = \frac{\int_{-\infty}^{E_F} ED(E) f_T'(E - E_F) dE}{\int_{-\infty}^{E_F} D(E) f_T'(E - E_F) dE} \quad (9)$$

where $D(E)$ is the density of states, and $-f_T'(E - E_F)$ is the derivative of the Fermi–Dirac distribution function $f_T(E - E_F) = \{exp[(E - E_F)/k_B T] + 1\}^{-1}$, used as an effective weight factor $w(E)$ to evaluate the contribution of every electronic state to the surface reaction. The spreading of the $w(E)$ is sensitive to the magnitude of $k_B T$, where k_B is the Boltzmann's constant and T is not the actual temperature but a parametric temperature [13, 42], and thus $k_B T$ serves as an adjustable parameter to tune the weight factor. As suggested by previous studies [13, 42], when $k_B T$ assumes a value of 0.4 eV, optimal correlation can be achieved between D_F and the surface

bonding and reactivity, and in particular, ΔG_H of hydrogen adsorption would exhibit a linear trend with the D_F of the catalyst.

Guided by the above model, we then analyzed the relationship between HER activities of various sites at phase boundaries with their corresponding electronic structures. We started by examining the group of Te sites at $ZZ_{Mo} - \alpha - C| -$ and $ZZ_{Mo} - \beta - T| +$ boundaries. Fig. 4(b) plots the D_F values of various Te sites versus corresponding ΔG_H values. An apparent linear relation between D_F and ΔG_H can be observed, with a larger D_F indicating stronger H-Te bonding. This suggests that D_F serve as a good metric to quantify the HER activity of Te sites at $MoTe_2$ phase boundaries. The Fermi-abundance model is also expected to apply to a broad class of other adsorption sites in both phase boundaries and pristine lattices, where hydrogen predominately interacts with a single host atom at the adsorption site (see below for further discussion) [13, 43].

However, despite the success of the Fermi-abundance model in describing the Te sites, it fails to yield good representation of the HER activity for other sites, i.e., the Mo and hollow sites, at $MoTe_2$ phase boundaries, as demonstrated in Fig. S7 (see Supporting Information). This indicates clear limitation of the Fermi-abundance model. To understand such limitation, we took a closer look at those Mo and hollow sites at phase boundaries. For insights into how hydrogen interacts with atoms at different sites, we examined the charge distribution contour associated with hydrogen adsorption, based on the spatial charge density difference $\Delta\rho(\boldsymbol{r})$:

$$\Delta\rho(\boldsymbol{r}) = \rho_{PB-H}(\boldsymbol{r}) - \rho_{PB}(\boldsymbol{r}) - \rho_H(\boldsymbol{r}) \quad (9)$$

where $\rho_{PB-H}(\boldsymbol{r})$and $\rho_{PB}(\boldsymbol{r})$ are the space charge densities of the phase boundaries with and without hydrogen adsorption, at location $\boldsymbol{r}$. $\rho_H(\boldsymbol{r})$ is the electron charge density of an hydrogen atom at the same position in a reference pristine supercell. The obtained charge distribution contours of phase boundaries with H adsorbed on Te1, Mo1 and HL1 sites are shown in Fig. 5(a)-(c) as representatives of three types of adsorption sites (See Figs S8 and S9 in Supporting Information for the charge distributions of other adsorption configurations). The yellow and cyan colors in the contour signal gain and loss of charges respectively, indicative of the overlap of various orbitals from different atoms. For adsorption at the Te1 site, we see from Fig. 5(a) that hydrogen mostly interacts with the Te atom alone, showing a clear charge gain to hydrogen from Te, whereas the interactions between hydrogen and other atoms are negligible. Now examining

the Mo1 site, we see from Fig. 5(b) that hydrogen not only interacts with the Mo atom, but also with the surrounding Te atoms. Apart from a charge transfer from Mo and H atom, there is an apparent loss of charges from neighbor Te atoms to H atom. The difference in local atomic interactions at Te1 and Mo1 sites are also well reflected in the DOS plots. As seen from Fig. 5(d), one can see that for the Te1 site, only the states of Te atom diminish significantly upon hydrogen adsorption. The 5s and 5p states of the Te atom hybrid with 1s state of hydrogen to result in the energy splitting and the formation of new bonding states. In comparison, for the Mo1 site, decrease in the states of both Mo and Te atoms near the Fermi level can be observed. The hybridization of 1s state of hydrogen with 5s and 5p bonding states of Te atom and 4d bonding states of Mo atom results in the formation of new bonding states. Therefore, with multiple orbitals from different atoms taken part in the interaction between the H atom and the catalyst, the Fermi-abundance model is no longer suitable to describe HER activity for Mo sites. Nonetheless, despite quantitative assessment of the activation at Mo sites being not possible, qualitative evaluation based on the DOS plots is possible. As shown in Fig. S10 (see Supporting Information), Mo sites in phase boundaries have more occupied states near the E_F compared to their counterparts in the pristine lattice, and thus expected to have stronger hydrogen adsorption.

Regarding the HL site, it resembles the Mo1 site in the fact that hydrogen adsorption also involves multiple atoms. As shown in Fig. 5(c), hydrogen adsorbed at the HL site is not sitting on top of an individual atom but in close vicinity with three adjacent Mo atoms along the x-y plane, showing a clear charge gain to hydrogen from these Mo atoms. Similar to what described above for the Mo1 site, hydrogen adsorption at the HL site may also be understood by examining the Mo atoms hydrogen interacts with. Fig. 5(d) shows the DOS plots of Mo and Te atoms after hydrogen adsorption at the HL1 site. We can see that the 4d states of the Mo atom hybridize with the 1s state of hydrogen, resulting in the formation of new bonding states, while the DOS of the Te atom remains nearly unchanged with no new bonding states formed post adsorption. Thus, the interaction between multiple Mo atoms and H atom occurs and causes the failure of the Fermi-abundance model to describe HER activity at the HL sites. However, the activations at HL sites can still be evaluated based on the DOS plots of Mo atoms (See Fig. S10 in Supporting Information).

The above analysis of electronic structures provides us with critical insights for assessing hydrogen adsorption. However, there remains a puzzle why only HL sites exhibit optimal adsorption performance (with near zero ΔG_H, cf. Fig. 3). Fig. 6 shows the projected density of states (pDOS) of 4d orbitals of the Mo atom (i.e., the Mo1 atom) shared by the Mo1 and HL1 sites, for hydrogen adsorption at the Mo1 and HL1 sites respectively. One can see that 4d states yield a high peak near the Fermi level (prior to hydrogen adsorption), indicating its great contribution to the bonding. Specifically, these orbitals are dxy and $dx^2 - y^2$ orbitals. In order to form a strong bonding upon hydrogen adsorption, it is preferable to have an overlap between the 1s orbital of hydrogen and dxy or $dx^2 - y^2$ orbital of the Mo atom, while overlapping between 1s of hydrogen and other d orbitals (e.g. dz^2) of Mo is less desirable and would render the Mo-H bond weaker.

Upon hydrogen adsorption, we see from Fig. 5(b) that, for adsorption at the Mo1 site, the distribution of electronic charge shows an orbital character of dz^2, indicating a interaction between Mo dz^2 and hydrogen 1s. Also, from the pDOS plot in Fig. 6, we can see that the new 4d bonding state post hydrogen adsorption at the Mo1 site mainly originates from the dz^2 states. In contrast, for hydrogen adsorption at the HL1 site, it mainly interacts with the d orbitals of three adjacent Mo atoms parallel with the xy plane, i.e. dxy or $dx^2 - y^2$ orbitals (cf. Fig. 5(c)), with the distribution of electronic charge of Mo atoms showing apparent $dx^2 - y^2$ and dxy characters. In accordance, as seen from the pDOS plot in Fig. 6, $dx^2 - y^2$ orbital contributes most to the formation of 4d bonding states for the case of the HL1 site (for another Mo atom neighboring the HL1 site, dxy orbital contributes most to the formation of 4d bonding states, see Fig. S11 in Supporting Information). These bonding correspond to the strong hydrogen adsorption, hence optimal hydrogen adsorption at HL sites.

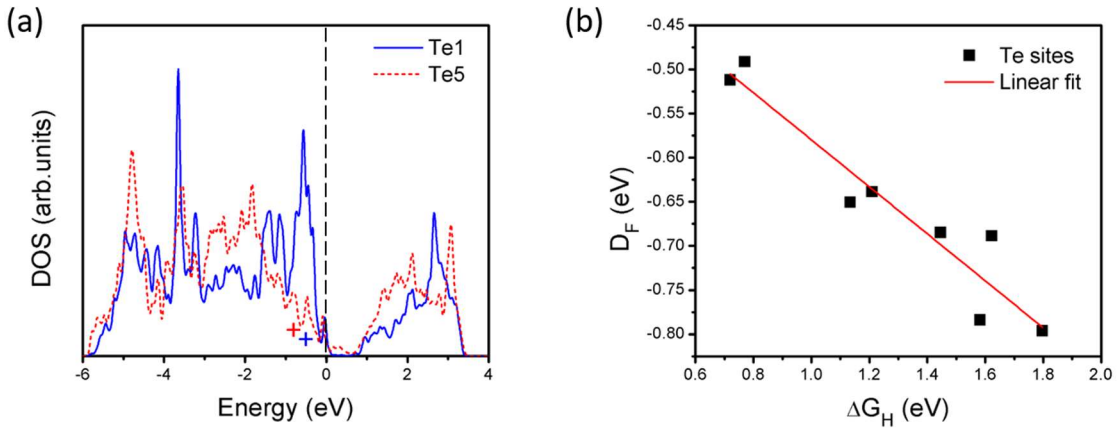

Fig. 4 (a) DOS of two representative Te atoms for H adsorption sites. The symbol "+" labels the position of Fermi-abundance center (D_F). (b) Relationship between D_F values and ΔG_H for Te atoms.

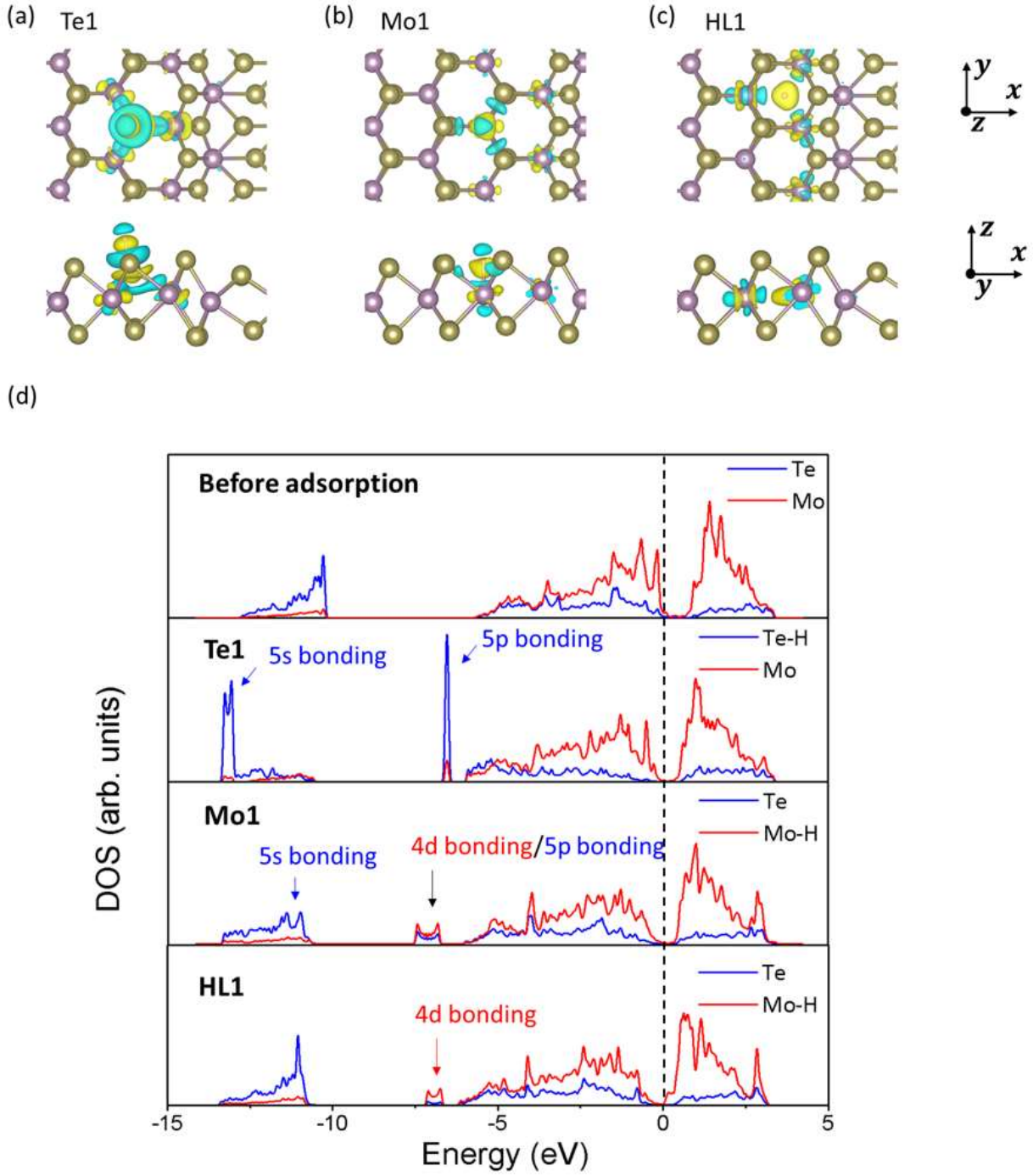

Fig. 5 Charge distribution contour plots for hydrogen adsorption sites (a) Te1, (b) Mo1 and (c) HL1 sites at the $MoTe_2$ phase boundary. The yellow and cyan surfaces correspond to gain and loss of charge respectively, with isosurface of 0.003e/Å^3. (d) DOS plots for Te and Mo atoms respectively (top panel)

before hydrogen adsorption, (second panel) after hydrogen adsorption on Te1 site, (third panel) after hydrogen adsorption at the Mo1 site, and (bottom panel) after hydrogen adsorption at the HL1 site.

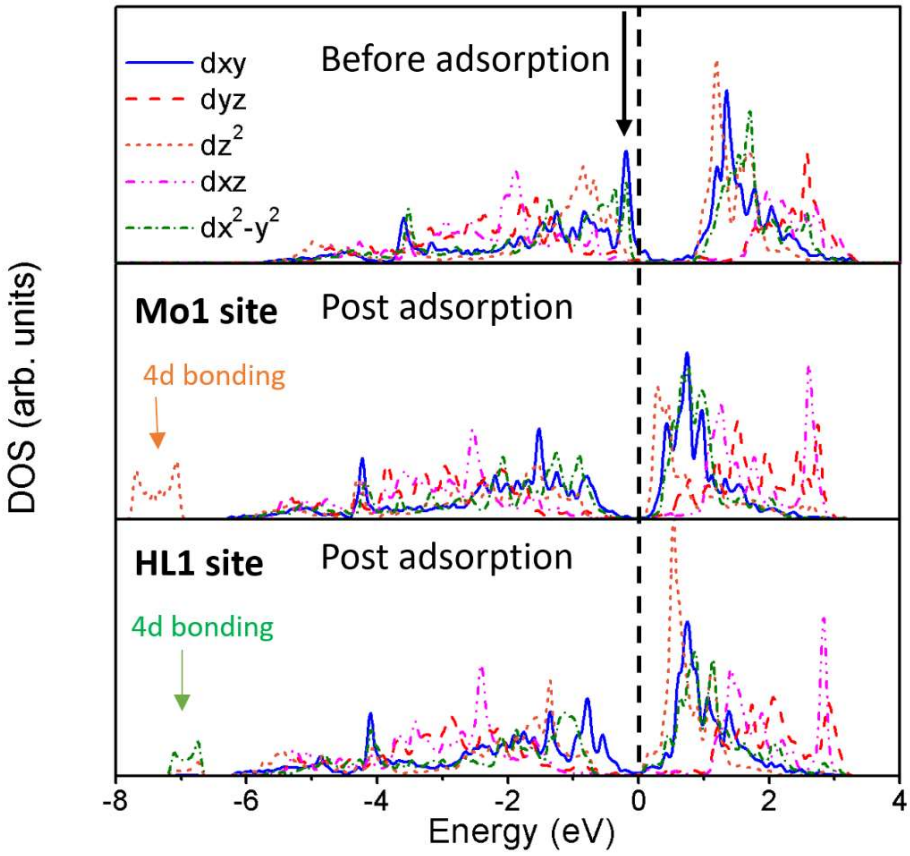

Fig. 6 Projected DOS (pDOS) plots for the d orbitals of the Mo1 atom along the $MoTe_2$ phase boundary, (top panel) before adsorption, after adsorption on Mo1 site, and after adsorption on HL1 site. Black arrow indicates the reinforcing states of dxy and $dx^2 - y^2$ orbitals near the Fermi level.

CONCLUSION

In summary, comprehensive first-principles calculations have been performed to investigate HER activities at phase boundaries in TMDC, using $MoTe_2$ as a representative. Possible 2H/1T' phase boundaries have been constructed, with their structural stability and formation energies examined to identify stable configurations. Three categories of sites, namely Te, Mo and hollow sites, in energetically stable phase boundaries were identified as potential catalytic centers for HER.

All those sites were demonstrated to activate hydrogen adsorption by reducing the magnitude of the Gibbs free energy ΔG_H, promising to enhance HER activity. In particular, the hollow sites were found to exhibit ΔG_H near the thermoneutral value, comparable to that of Pt at moderate hydrogen coverages. The mechanisms underlying such activation at phase boundaries were then revealed, and found to be attributed to the unique local hydrogen adsorption geometries and electronic structures at phase boundaries. Specifically, for the Te sites where hydrogen interacts almost solely with the host atom (i.e., Te), the catalytic activity is well understood and predicted by the Fermi-abundance model. The Fermi-abundance model and similar interpretation are also expected to apply to a broad class of other adsorption sites in both phase boundaries and pristine lattices, where hydrogen predominately interacts with a single host atom at the adsorption site. However, the Fermi-abundance model breaks down for the Mo and hollow sites where hydrogen adsorption assumes a more complex geometry and involves multiple atoms, though qualitative assessment can still be made by analyzing the local charge distribution and density of states. In addition, we elucidated that the optimal hydrogen adsorption performance at hollow sites originates from the fact that the phase boundary modifies the d_{xy} and $d_{x^2-y^2}$ orbitals of Mo atoms, thus giving rise to much stronger binding with hydrogen.

Our study demonstrates a viable pathway to activate the basal plane of 2D TMDCs for HER through phase boundary engineering and clarifies the important mechanistic aspects underlying hydrogen activation at phase boundaries, providing valuable theoretical insights towards designing new class of high-performance HER electrocatalysts based on 2D TMDCs.

ASSOCIATED CONTENT

Supporting Information

Discussions of benchmark studies on nanoribbon models, calculation details for formation energy of zigzag phase boundaries, discussions of local bond variation at the phase boundaries, figures of adsorption sites of pristine 2H and 1T' $MoTe_2$, figures of hydrogen adsorption configurations at HL sites, figures of DOS of Te and Mo sites in phase boundaries, discussions of the Fermi-abundance model for Mo sites, figures of the charge distribution at various adsorption sites along phase boundaries, and figures of projected DOS for d orbitals of Mo2 atoms (PDF).

AUTHOR INFORMATION

Corresponding Author: *E-mail: jun.song2@mcgill.ca.

Notes: The authors declare no competing financial interest.

ACKNOWLEDGMENTS

This research is supported by the Natural Sciences and Engineering Research Council of Canada (NSERC) Discovery Grant (grant #: NSERC RGPIN-2017-05187), and the McGill Engineering Doctoral Award (MEDA). The authors would also like to acknowledge the Compute Canada and Calcul Québec for providing computing resources.

REFERENCES

1. Turner, J. A., Sustainable Hydrogen Production. *Science* **2004,** *305* (5686), 972-974.

2. Trasatti, S., Work function, electronegativity, and electrochemical behaviour of metals: III. Electrolytic hydrogen evolution in acid solutions. *Journal of Electroanalytical Chemistry and Interfacial Electrochemistry* **1972,** *39* (1), 163-184.

3. Cheng, N.; Stambula, S.; Wang, D.; Banis, M. N.; Liu, J.; Riese, A.; Xiao, B.; Li, R.; Sham, T. K.; Liu, L. M.; Botton, G. A.; Sun, X., Platinum single-atom and cluster catalysis of the hydrogen evolution reaction. *Nat Commun* **2016,** *7*, 13638.

4. Jiao, Y.; Zheng, Y.; Jaroniec, M.; Qiao, S. Z., Design of electrocatalysts for oxygen- and hydrogen-involving energy conversion reactions. *Chem Soc Rev* **2015,** *44* (8), 2060-86.

5. Laursen, A. B.; Kegnæs, S.; Dahl, S.; Chorkendorff, I., Molybdenum sulfides—efficient and viable materials for electro-and photoelectrocatalytic hydrogen evolution. *Energy & Environmental Science* **2012,** *5* (2), 5577-5591.

6. Jaramillo, T. F.; Jørgensen, K. P.; Bonde, J.; Nielsen, J. H.; Horch, S.; Chorkendorff, I., Identification of active edge sites for electrochemical H2 evolution from MoS2 nanocatalysts. *science* **2007,** *317* (5834), 100-102.

7. Hinnemann, B.; Moses, P. G.; Bonde, J.; Jørgensen, K. P.; Nielsen, J. H.; Horch, S.; Chorkendorff, I.; Nørskov, J. K., Biomimetic hydrogen evolution: MoS2 nanoparticles as catalyst for hydrogen evolution. *Journal of the American Chemical Society* **2005,** *127* (15), 5308-5309.

8. An, Y. R.; Fan, X. L.; Luo, Z. F.; Lau, W. M., Nanopolygons of Monolayer MS2: Best Morphology and Size for HER Catalysis. *Nano Lett* **2017,** *17* (1), 368-376.

9. Hinnemann, B.; Moses, P. G.; Bonde, J.; Jørgensen, K. P.; Nielsen, J. H.; Horch, S.; Chorkendorff, I.; Nørskov, J. K., Biomimetic Hydrogen Evolution: MoS2 Nanoparticles as Catalyst for Hydrogen Evolution. *Journal of the American Chemical Society* **2005,** *127* (15), 5308-5309.

10. Chen, Y.; Yang, K.; Jiang, B.; Li, J.; Zeng, M.; Fu, L., Emerging two-dimensional nanomaterials for electrochemical hydrogen evolution. *Journal of Materials Chemistry A* **2017,** *5* (18), 8187-8208.

11. Zhu, C. R.; Gao, D.; Ding, J.; Chao, D.; Wang, J., TMD-based highly efficient electrocatalysts developed by combined computational and experimental approaches. *Chem Soc Rev* **2018,** *47* (12), 4332-4356.

12. Ouyang, Y.; Ling, C.; Chen, Q.; Wang, Z.; Shi, L.; Wang, J., Activating Inert Basal Planes of MoS2 for Hydrogen Evolution Reaction through the Formation of Different Intrinsic Defects. *Chemistry of Materials* **2016,** *28* (12), 4390-4396.

13. Shu, H.; Zhou, D.; Li, F.; Cao, D.; Chen, X., Defect Engineering in MoSe2 for the Hydrogen Evolution Reaction: From Point Defects to Edges. *ACS Appl Mater Interfaces* **2017,** *9* (49), 42688-42698.

14. Tsai, C.; Chan, K.; Abild-Pedersen, F.; Norskov, J. K., Active edge sites in MoSe2 and WSe2 catalysts for the hydrogen evolution reaction: a density functional study. *Phys Chem Chem Phys* **2014,** *16* (26), 13156-64.

15. Zhu, J.; Wang, Z. C.; Dai, H.; Wang, Q.; Yang, R.; Yu, H.; Liao, M.; Zhang, J.; Chen, W.; Wei, Z.; Li, N.; Du, L.; Shi, D.; Wang, W.; Zhang, L.; Jiang, Y.; Zhang, G., Boundary activated hydrogen evolution reaction on monolayer MoS2. *Nat Commun* **2019,** *10* (1), 1348.

16. Voiry, D.; Salehi, M.; Silva, R.; Fujita, T.; Chen, M.; Asefa, T.; Shenoy, V. B.; Eda, G.; Chhowalla, M., Conducting MoS(2) nanosheets as catalysts for hydrogen evolution reaction. *Nano Lett* **2013,** *13* (12), 6222-7.

17. Lukowski, M. A.; Daniel, A. S.; Meng, F.; Forticaux, A.; Li, L.; Jin, S., Enhanced hydrogen evolution catalysis from chemically exfoliated metallic MoS2 nanosheets. *J Am Chem Soc* **2013,** *135* (28), 10274-7.

18. Tang, Q.; Jiang, D.-e., Mechanism of Hydrogen Evolution Reaction on 1T-MoS2 from First Principles. *ACS Catalysis* **2016,** *6* (8), 4953-4961.

19. Calandra, M., Chemically exfoliated single-layer MoS 2: Stability, lattice dynamics, and catalytic adsorption from first principles. *Physical Review B* **2013,** *88* (24), 245428.

20. Wang, D.; Zhang, X.; Bao, S.; Zhang, Z.; Fei, H.; Wu, Z., Phase engineering of a multiphasic 1T/2H MoS2 catalyst for highly efficient hydrogen evolution. *Journal of Materials Chemistry A* **2017,** *5* (6), 2681-2688.

21. Sung, J. H.; Heo, H.; Si, S.; Kim, Y. H.; Noh, H. R.; Song, K.; Kim, J.; Lee, C. S.; Seo, S. Y.; Kim, D. H.; Kim, H. K.; Yeom, H. W.; Kim, T. H.; Choi, S. Y.; Kim, J. S.; Jo, M. H., Coplanar semiconductor-metal circuitry defined on few-layer MoTe2 via polymorphic heteroepitaxy. *Nat Nanotechnol* **2017,** *12* (11), 1064-1070.

22. Duerloo, K. A.; Reed, E. J., Structural Phase Transitions by Design in Monolayer Alloys. *ACS Nano* **2016,** *10* (1), 289-97.

23. Li, A.; Pan, J.; Dai, X.; Ouyang, F., Electrical contacts of coplanar 2H/1T′ MoTe2 monolayer. *Journal of Applied Physics* **2019,** *125* (7).

24. Zhou, L.; Xu, K.; Zubair, A.; Zhang, X.; Ouyang, F.; Palacios, T.; Dresselhaus, M. S.; Li, Y.; Kong, J., Role of Molecular Sieves in the CVD Synthesis of Large-Area 2D MoTe2. *Advanced Functional Materials* **2017,** *27* (3).

25. Luo, W.; Zhu, M.; Peng, G.; Zheng, X.; Miao, F.; Bai, S.; Zhang, X.-A.; Qin, S., Carrier Modulation of Ambipolar Few-Layer MoTe2 Transistors by MgO Surface Charge Transfer Doping. *Advanced Functional Materials* **2018,** *28* (15), 1704539.

26. Bie, Y. Q.; Grosso, G.; Heuck, M.; Furchi, M. M.; Cao, Y.; Zheng, J.; Bunandar, D.; Navarro-Moratalla, E.; Zhou, L.; Efetov, D. K.; Taniguchi, T.; Watanabe, K.; Kong, J.; Englund, D.; Jarillo-Herrero, P., A MoTe2-based light-emitting diode and photodetector for silicon photonic integrated circuits. *Nat Nanotechnol* **2017,** *12* (12), 1124-1129.

27. Zhou, Y.; Silva, J. L.; Woods, J. M.; Pondick, J. V.; Feng, Q.; Liang, Z.; Liu, W.; Lin, L.; Deng, B.; Brena, B.; Xia, F.; Peng, H.; Liu, Z.; Wang, H.; Araujo, C. M.; Cha, J. J., Revealing the Contribution of Individual Factors to Hydrogen Evolution Reaction Catalytic Activity. *Adv Mater* **2018,** *30* (18), e1706076.

28. Keum, D. H.; Cho, S.; Kim, J. H.; Choe, D.-H.; Sung, H.-J.; Kan, M.; Kang, H.; Hwang, J.-Y.; Kim, S. W.; Yang, H.; Chang, K. J.; Lee, Y. H., Bandgap opening in few-layered monoclinic MoTe2. *Nature Physics* **2015,** *11*, 482.

29. Yin, Y.; Han, J.; Zhang, Y.; Zhang, X.; Xu, P.; Yuan, Q.; Samad, L.; Wang, X.; Wang, Y.; Zhang, Z.; Zhang, P.; Cao, X.; Song, B.; Jin, S., Contributions of Phase, Sulfur Vacancies, and Edges to the Hydrogen Evolution Reaction Catalytic Activity of Porous Molybdenum Disulfide Nanosheets. *J Am Chem Soc* **2016,** *138* (25), 7965-72.

30. Zhao, N.; Wang, L.; Zhang, Z.; Li, Y., Activating the MoS2 Basal Planes for Electrocatalytic Hydrogen Evolution by 2H/1T' Structural Interfaces. *ACS Appl Mater Interfaces* **2019,** *11* (45), 42014-42020.

31. Zhao, W.; Ding, F., Energetics and kinetics of phase transition between a 2H and a 1T MoS2 monolayer-a theoretical study. *Nanoscale* **2017,** *9* (6), 2301-2309.

32. Zhou, S.; Han, J.; Sun, J.; Srolovitz, D. J., MoS2 edges and heterophase interfaces: energy, structure and phase engineering. *2D Materials* **2017,** *4* (2).

33. Kresse, G.; Joubert, D., From ultrasoft pseudopotentials to the projector augmented-wave method. *Physical Review B* **1999,** *59* (3), 1758-1775.

34. Kresse, G.; Furthmüller, J., Efficient iterative schemes for ab initio total-energy calculations using a plane-wave basis set. *Physical Review B* **1996,** *54* (16), 11169-11186.

35. Blöchl, P. E., Projector augmented-wave method. *Physical Review B* **1994,** *50* (24), 17953-17979.

36. Perdew, J. P.; Burke, K.; Ernzerhof, M., Generalized Gradient Approximation Made Simple. *Physical Review Letters* **1996,** *77* (18), 3865-3868.

37. Perdew, J. P.; Chevary, J. A.; Vosko, S. H.; Jackson, K. A.; Pederson, M. R.; Singh, D. J.; Fiolhais, C., Atoms, molecules, solids, and surfaces: Applications of the generalized gradient approximation for exchange and correlation. *Physical Review B* **1992,** *46* (11), 6671-6687.

38. Grimme, S.; Antony, J.; Ehrlich, S.; Krieg, H., A consistent and accurate ab initio parametrization of density functional dispersion correction (DFT-D) for the 94 elements H-Pu. *The Journal of Chemical Physics* **2010,** *132* (15), 154104.

39. Grimme, S.; Ehrlich, S.; Goerigk, L., Effect of the damping function in dispersion corrected density functional theory. *Journal of Computational Chemistry* **2011,** *32* (7), 1456-1465.

40. Nørskov, J. K.; Bligaard, T.; Logadottir, A.; Kitchin, J. R.; Chen, J. G.; Pandelov, S.; Stimming, U., Trends in the Exchange Current for Hydrogen Evolution. *Journal of The Electrochemical Society* **2005,** *152* (3), J23-J26.

41. Tsai, C.; Abild-Pedersen, F.; Nørskov, J. K., Tuning the MoS2 Edge-Site Activity for Hydrogen Evolution via Support Interactions. *Nano Letters* **2014,** *14* (3), 1381-1387.

42. Huang, B.; Xiao, L.; Lu, J.; Zhuang, L., Spatially Resolved Quantification of the Surface Reactivity of Solid Catalysts. *Angewandte Chemie International Edition* **2016,** *55* (21), 6239-6243.

43. Zhang, Y.; Chen, X.; Huang, Y.; Zhang, C.; Li, F.; Shu, H., The Role of Intrinsic Defects in Electrocatalytic Activity of Monolayer VS2 Basal Planes for the Hydrogen Evolution Reaction. *The Journal of Physical Chemistry C* **2017,** *121* (3), 1530-1536.